Jülich Centre for Neutron Science JCNS and Peter Grünberg Institut PGI
JCNS-2 & PGI-4: Scattering Methods

Temperature Dependent Elastic Constants of Silicides investigated using Resonant Ultrasound Spectroscopy

Bachelorarbeit

Physical Engineering B. Eng.
Fachbereich Energietechnik
Fachhochschule Aachen, Campus Jülich

vorgelegt von

Tao Chen

Jülich, Januar 2014

Diese Arbeit ist von mir selbständig angefertigt und verfasst. Es sind keine anderen als die angegebenen Quellen und Hilfsmittel benutzt worden.

Unterschrift ______________________

Ort, Datum ______________________

Diese Arbeit wurde betreut von:

1. Prüfer Prof. Dr. rer. nat. Arnold Förster
2. Prüfer Dr. rer. nat. Benedikt Klobes

Contents

List of Figures

List of Tables

Chapter 1

Introduction

Global warming and rapid draining of oil are severe issues the world is facing today. Therefore, research for renewable energy (solar energy, wind power, biomass fuel, etc.) becomes more and more important. The utilization of waste heat produced by industrial processes is a comfortable way to provide energy. It is not only environmentally friendly, but can also reduce the greenhouse effect. Thermoelectric materials are used in thermoelectric devices for utilization of waste heat. The thermoelectric devices can directly convert temperature differences to electric voltage and vice versa. However, their energy conversion efficiency (ca. 10%) [1] is relatively low compared to traditional engines (e.g. the efficiency of a combined cycle power plant is around 60%). In order to raise the efficiency of thermoelectric devices, research for more efficient thermoelectric materials is required.

Transition metal silicides are cheap and environment friendly materials and interested thermoelectric materials include $FeSi_2$, $CrSi_2$, $Mn_{1.7}Si_2$, CoSi and Mg_2Si based compounds. Their property of excellent mechanical and chemical resistance make them interesting for application in high temperature power generation [2, 3]. Three parameters of thermoelectric materials have main impact on efficiency, i.e. Seebeck coefficient S, electrical conductivity σ and total thermal conductivity κ ($\kappa=\kappa_e+\kappa_l$ the sum of the electronic κ_e and the lattice contribution κ_l, respectively). During this work, our focus is on the determination of temperature dependent lattice thermal conductivity κ_l of two types silicide materials, i.e. n-type semiconductor material $Mg_2Si_{0.4}Sn_{0.6}$ and p-type semiconductor material $MnSi_{1.85}$.

Using RUS we first measured the resonant frequencies of both thermoelectric materials from room temperature to high temperature and then extracted their elastic moduli using a computer program (based on Levenberg-Marquardt algorithm). In order to take measurement at different set temperature, development for a program to control temperature is also required.

Chapter 2

Thermoelectricity

This chapter presents a brief introduction to thermoelectricity and properties of thermoelectric materials.

2.1 Introduction

Electricity generated directly from heat is known as thermoelectricity. This thermoelectric effect, named and discovered in 1821 by German physicist Thomas J. Seebeck, corresponds to the appearance of an electric potential if junctions between conductors are placed in a thermal gradient.

In 1834 Jean-Charles Peltier reported the second of the thermoelectric effects. He discovered that when an electric current flows across a junction heating or cooling of the junction takes place depending on the direction of the current. Both the Seebeck and the Peltier effect occur only in junctions between different materials [3].

In 1855 William Thomson (often referred to simply as Lord Kelvin) discovered the connection between Seebeck and Peltier phenomena. He established a relationship between the coefficients that describe the Seebeck and Peltier effects by applying the theory of thermodynamics. His theory also showed that there must be a third thermoelectric effect, which exists in a homogeneous conductor. The effect, known as the Thomson effect, describes that in a single electric conductor subjected to a temperature gradient an electromotive force appears, and conversely, the electrical current resulting from application of an emf is accompanied by a heat current [4].

All these discoveries have been used in devices using suitable thermoelectric materials nowadays, e.g. thermoelectric generators (also called Seebeck generators) which convert heat directly into electrical energy, thermoelectric refrigeration devices (Peltier cooler) which pump heat using an electric current and thermocouples in temperature sensors. These devices have undisputed advantages: absence of mechanical motion that significantly reduces aging, the noiseless operation, and the absence of scaling effect [3]. But due to the materials properties, the energy conversion efficiency is relatively low. Therefore, research for more efficient thermoelectric materials is required. In the next section we will talk about properties of thermoelectric materials and discuss which parameters have impact on the efficiency.

2.2 Thermoelectric Materials

All materials show the thermoelectric effect, but in most materials it is too small to be useful. Thermoelectric materials show the thermoelectric effect in a strong or convenient form and thus can be used in thermoelectric devices.

Three factors have main effect on the performance of thermoelectric materials:

- The Seebeck coefficient S [unit V/K].
- The electrical conductivity σ [unit S/m].
- The total thermal conductivity κ (κ=κ_e+κ_l the sum of the electronic κ_e and the lattice contribution κ_l, respectively) [unit W/(m· K)].

These three factors are usually incorporated in one material parameter

$$Z = \frac{S^2 \cdot \sigma}{\kappa}, \tag{2.1}$$

where Z is called the **figure of merit** [unit K^{-1}]. Because Z is temperature dependent, the dimensionless figure of merit ZT is more commonly used. Efficient thermoelectric materials usually have $Z > 0.003\text{K}^{-1}$ and $ZT > 1$ [1].

Ideal thermoelectric materials have a high value of ZT, which means that the materials should have high values of Seebeck coefficient S and electrical conductivity, but a low value of total thermal conductivity κ. To find such a proper material is a quite complex problem, because the three factors are not independent. For solid materials, S usually increases with decreasing σ.

When the factor σ increases, the factor κ also increases. For instance, metals normally have a high value of electrical conductivity σ, but according to the *Wiedemann-Franz Law* $\kappa = L \cdot T \cdot \sigma$ (here L is the Lorenz number and T is the temperature) [5], they will also exhibit a high value of thermal conductivity κ. Therefore, the quest for high ZT materials is a great challenge nowadays.

In this work, the silicides $Mg_2Si_{0.4}Sn_{0.6}$ and $MnSi_{1.85}$ were chosen to investigate because they are not only cheap and environment friendly, but also have excellent mechanical and chemical resistance property which makes them interesting for application in high temperature power generation [2].

2.3 Thermoelectric Generator

Thermoelectric generators, as indicated in section 2.1, are the devices that convert wasted excess heat energy (temperature gradient) directly into electrical energy. Figure 2.1 shows a typical thermoelectric module. To make a thermoelectric generator, typically we connect many thermoelectric couples of n-type and p-type thermoelectric semiconductors (Figure 2.2) electrically in series and thermally in parallel.

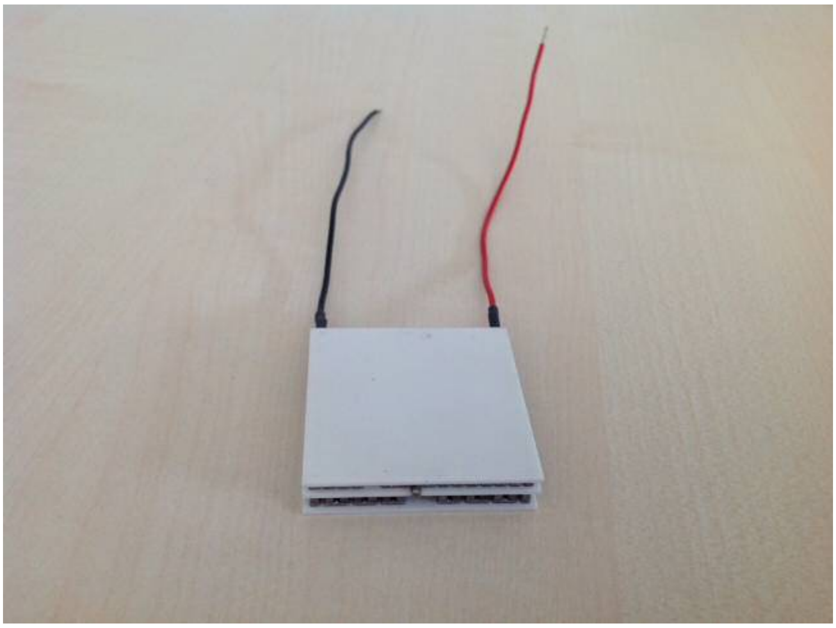

Figure 2.1: A typical thermoelectric generator module.

Thermoelectric generators have many advantages: they contain no moving

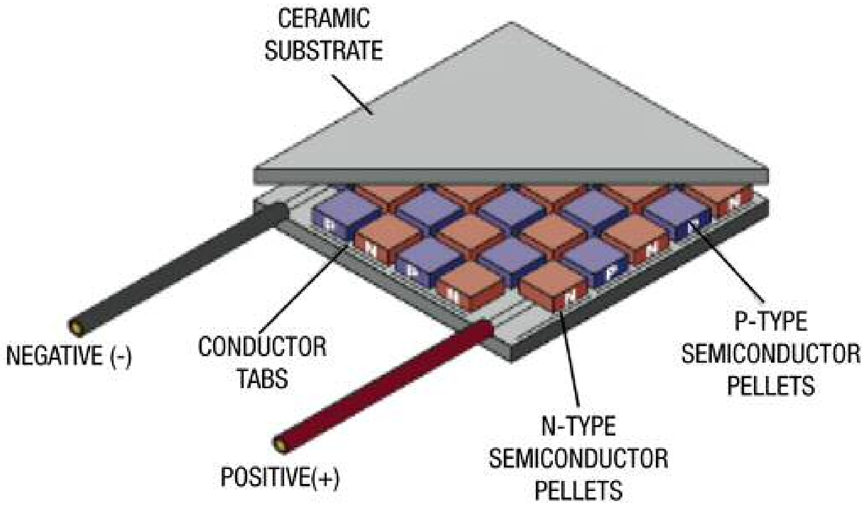

Figure 2.2: Construction of thermoelectric generator module. Figure taken from [6].

parts, recycle wasted heat and operate quietly. But compared to traditional engines they have lower efficiency. To find materials with good efficiency, which means to find materials with high value of ZT, we have many aspects to consider. One aspect is the determination of the temperature dependency of lattice thermal conductivity κ_l which is the focus in this investigation. How to find the relationship between κ_l and temperature? Well, with the Debye model, the lattice thermal conductivity is given by

$$\kappa_l \approx \frac{1}{3} c_v v_s \lambda_{ph} = \frac{1}{3} c_v v_s^2 \tau_{ph}, \tag{2.2}$$

where c_v is the lattice specific heat, v_s the speed of sound, λ_{ph} and τ_{ph} the phonon mean free path and mean free life time, respectively [3]. Because the phonon mean free life stays almost constant as temperature changes, we will try to investigate the change of speed of sound with temperature. In the next chapter we will discuss how we solve this problem.

Chapter 3

Elasticity

Since the speed of sound in a material depends on the so called elastic tensor of the material, its temperature dependence is reflected in temperature dependent elastic constants. Before the method of how the elastic constants can be experimentally accessed is described, the relationship between speed of sound and elastic constants will be presented in this chapter.

3.1 Introduction

If we apply forces on a material, then a deformation will occur. If the deformation does not exceed a certain limit, the material will return to the original shape after being deformed. This property of material is called elasticity.

The physical reason for elastic properties is quite different for different materials. Basically, it is caused by interatomic forces acting on atoms when they are displaced from their equilibrium positions. Figure 3.1 shows a typical interatomic potential energy curve.
Using a Taylor series, the potential energy near the position $r = r_0$ can be written in the form of

$$U(r) = U_0 + \frac{U'(r_0)}{1!}(r - r_0) + \frac{U''(r_0)}{2!}(r - r_0)^2 + \frac{U'''(r_0)}{1!}(r - r_0)^3 + \cdots \,. \quad (3.1)$$

We take only the first 3 terms (further can be ignored) and at the equilibrium position $r = r_0$, $U'(r_0) = 0$, so we get

$$U(r) = U_0 + \frac{U''(r_0)}{2!}(r - r_0)^2. \quad (3.2)$$

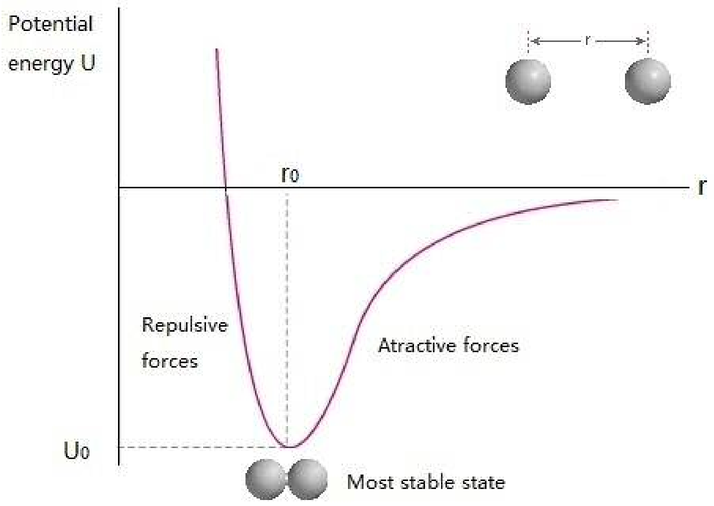

Figure 3.1: A typical binding curve has a minimum potential energy at the equilibrium interatomic distance r_0. Figure adopted from [7].

Using the relationship between force F and potential energy, i.e. $F = -\frac{\mathrm{d}U}{\mathrm{d}r}$, we obtain force F acting on an atom

$$F = -\frac{\mathrm{d}U}{\mathrm{d}r} = -U''(r_0)(r - r_0), \tag{3.3}$$

where $U''(r_0)$ is a constant. We define $k = U''(r_0)$ as an interatomic force constant and $u = r - r_0$ is the displacement of an atom from equilibrium position. Thus, Eq. (3.3) can be written in the form $F = -ku$, which represents the simplest expression for the *Hooke's Law* that shows the force acting on an atom. For homogeneous and isotropic materials, the *Hooke's Law* is accurate enough to describe the relation between the forces and deformations in a certain limit [8].

3.1.1 Stress

The definition of stress in mechanics is like pressure. In general, the force per unit area, acting perpendicular to the surface is defined as the **normal stress** and to the tangent of the surface is called **shear stress**. This is shown in Figure 3.2, which is the general state of stress. We can write these stresses in a form of σ_{ij}. This means, the force is applied on "i" face in "j" direction. Here obviously the normal stresses are components σ_{xx}, σ_{yy}, σ_{zz} and the shear stresses are components σ_{xy}, σ_{xz}, σ_{yx}, σ_{yz}, σ_{zx}, σ_{zy}.

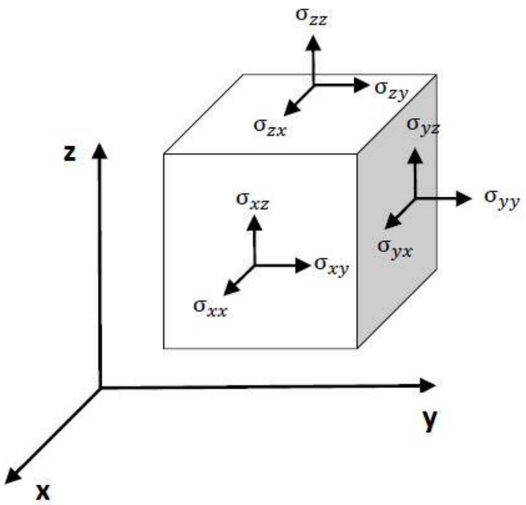

Figure 3.2: Stresses acting on a cubic volume element of a material.

Since the body must be in equilibrium (resultant force $\boldsymbol{R} = \Sigma \boldsymbol{F}_i = \boldsymbol{0}$ and resultant moment $\boldsymbol{M}_R = \Sigma \boldsymbol{M}_i = \boldsymbol{0}$), we must have

$$\sigma_{ij} = \sigma_{ji}. \tag{3.4}$$

These components at any point inside a material can be arranged in the form of a matrix, which is called Cauchy stress tensor σ:

$$\sigma = \begin{pmatrix} \sigma_{xx} & \sigma_{xy} & \sigma_{xz} \\ \sigma_{yx} & \sigma_{yy} & \sigma_{yz} \\ \sigma_{zx} & \sigma_{zy} & \sigma_{zz} \end{pmatrix}. \tag{3.5}$$

This matrix is symmetric because of $\sigma_{ij} = \sigma_{ji}$ and will be used later.

3.1.2 Strain

As already indicated, when we apply force on an object, a deformation will occur. For example, consider we have a straight bar with undeformed length L_0 (Figure 3.3) and we apply force on it. The **normal strain** is given by the equation $\varepsilon = \frac{\Delta L}{L_0}$. This equation is valid only if ε is constant over the entire length of the bar. Now we consider an infinitesimal rectangle $ABCD$, which is transformed to $abcd$ (Figure.3.4). The displacement vector $\boldsymbol{u}$ depends on the point (x, y). Here for point $A(x, y)$ it has components $u_x(x, y)$ and $u_y(x, y)$

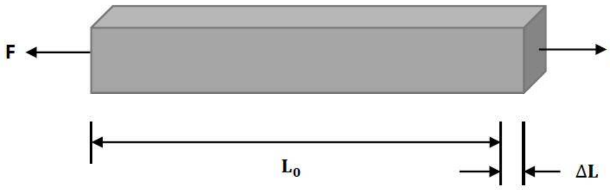

Figure 3.3: A straight bar with undeformed length L_0

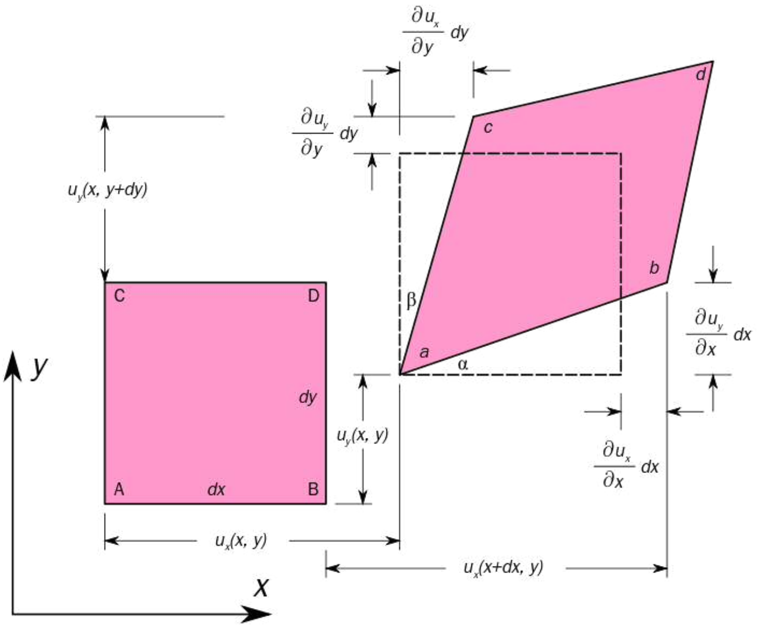

Figure 3.4: Two-dimensional geometric deformation of an infinitesimal material element.

in x- and in y-direction, respectively. For the functions u_x and u_y, which depend on the two variables x and y, we obtain

$$u_x(x + \mathrm{d}x, y + \mathrm{d}y) = u_x(x, y) + \frac{\partial u_x(x, y)}{\partial x}\mathrm{d}x + \frac{\partial u_x(x, y)}{\partial y}\mathrm{d}y + \cdots ,$$

$$u_y(x + \mathrm{d}x, y + \mathrm{d}y) = u_y(x, y) + \frac{\partial u_y(x, y)}{\partial x}\mathrm{d}x + \frac{\partial u_y(x, y)}{\partial y}\mathrm{d}y + \cdots .$$

Using these formulas, we now obtain the displacement of point B in x-direction (higher order terms are neglected)

$$u_x(x + \mathrm{d}x, y) = u_x + \frac{\partial u_x}{\partial x}\mathrm{d}x,$$

and displacement of point C in y-direction

$$u_y(x, y + \mathrm{d}y) = u_y + \frac{\partial u_y}{\partial y}\mathrm{d}y.$$

After the deformation, side $\overline{AB}$ became $\overline{ab}$. Since the deformation is very small, we assume $\alpha \ll 1$. So the length of $\overline{ab}$ is:

$$\overline{ab} = x + u_x + \frac{\partial u_x}{\partial x}\mathrm{d}x - u_x = \mathrm{d}x + \frac{\partial u_x}{\partial x}\mathrm{d}x.$$

As indicated before, the normal strain in x-direction of the rectangular element is defined:

$$\varepsilon_{xx} = \frac{\overline{ab} - \overline{AB}}{\overline{AB}} = \frac{\mathrm{d}x + \frac{\partial u_x}{\partial x}\mathrm{d}x - \mathrm{d}x}{\mathrm{d}x} = \frac{\partial u_x}{\partial x}.$$

Similarly, the normal strain in y- and in z-direction is $\varepsilon_{yy} = \frac{\partial u_y}{\partial y}$ and $\varepsilon_{zz} = \frac{\partial u_z}{\partial z}$, respectively. Not only are the lengths of sides changed, but also the angle between the sides. For instance, the change in angle between $\overline{AB}$ and $\overline{AC}$ equals $\alpha+\beta$ and we have the geometric relations

$$\tan\alpha = \frac{\frac{\partial u_y}{\partial x}\mathrm{d}x}{\mathrm{d}x + \frac{\partial u_x}{\partial x}\mathrm{d}x} = \frac{\frac{\partial u_y}{\partial x}}{1 + \frac{\partial u_x}{\partial x}},$$

$$\tan\beta = \frac{\frac{\partial u_x}{\partial y}\mathrm{d}y}{\mathrm{d}y + \frac{\partial u_y}{\partial y}\mathrm{d}y} = \frac{\frac{\partial u_x}{\partial y}}{1 + \frac{\partial u_y}{\partial y}}.$$

For small deformations, i.e. $\alpha, \beta \ll 1$, $\epsilon_{xx}, \epsilon_{yy} \ll 1$, we obtain $\alpha = \frac{\partial u_y}{\partial x}$ and $\beta = \frac{\partial u_x}{\partial y}$. Finally, the total change of angle between $\overline{AB}$ and $\overline{AC}$ on x, y-plane is $\gamma_{xy} = \frac{\partial u_y}{\partial x} + \frac{\partial u_x}{\partial y}$, which is called **shear strain**. The subscripts x and y represents that γ_{xy} describes the angle change in x, y-plane. By interchanging x, y, u_x and u_y, it can be easily shown that $\gamma_{xy} = \gamma_{yx}$.
Similarly, the shear strain on x-z and y-z planes are

$$\gamma_{xz} = \gamma_{zx} = \frac{\partial u_z}{\partial x} + \frac{\partial u_x}{\partial z},$$

$$\gamma_{yz} = \gamma_{zy} = \frac{\partial u_z}{\partial y} + \frac{\partial u_y}{\partial z}.$$

These components can be also organized into a matrix which is called strain tensor ε:

$$\varepsilon = \begin{pmatrix} \varepsilon_{xx} & \varepsilon_{xy} & \varepsilon_{xz} \\ \varepsilon_{yx} & \varepsilon_{yy} & \varepsilon_{yz} \\ \varepsilon_{zx} & \varepsilon_{zy} & \varepsilon_{zz} \end{pmatrix} = \begin{pmatrix} \varepsilon_{xx} & \frac{1}{2}\gamma_{xy} & \frac{1}{2}\gamma_{xz} \\ \frac{1}{2}\gamma_{yx} & \varepsilon_{yy} & \frac{1}{2}\gamma_{yz} \\ \frac{1}{2}\gamma_{zx} & \frac{1}{2}\gamma_{zy} & \varepsilon_{zz} \end{pmatrix}. \tag{3.6}$$

3.1.3 Elastic Constants

So far, we know the stress and strain tensors, and now the elastic constants will be introduced. The elastic constants c relate the strain and stress in a linear form

$$\sigma_{ij} = \sum_{k=1}^{3}\sum_{l=1}^{3} c_{ijkl}\varepsilon_{kl}, \tag{3.7}$$

where the subscripts 1, 2, 3 refer to x, y, z axes, respectively. The matrix c in a most general form has 3×3×3×3 components, however, because of the symmetrical form of σ_{ij} and ε_{kl}, we only need to find 36 elastic constants. Therefore we write the general form

$$\begin{pmatrix} \sigma_{xx} \\ \sigma_{yy} \\ \sigma_{zz} \\ \sigma_{yz} \\ \sigma_{xz} \\ \sigma_{xy} \end{pmatrix} = \begin{pmatrix} c_{11} & c_{12} & c_{13} & c_{14} & c_{15} & c_{16} \\ c_{21} & c_{22} & c_{23} & c_{24} & c_{25} & c_{26} \\ c_{31} & c_{32} & c_{33} & c_{34} & c_{35} & c_{36} \\ c_{41} & c_{42} & c_{43} & c_{44} & c_{45} & c_{46} \\ c_{51} & c_{52} & c_{53} & c_{54} & c_{55} & c_{56} \\ c_{61} & c_{62} & c_{63} & c_{64} & c_{65} & c_{66} \end{pmatrix} \begin{pmatrix} \varepsilon_{xx} \\ \varepsilon_{yy} \\ \varepsilon_{zz} \\ \varepsilon_{yz} \\ \varepsilon_{xz} \\ \varepsilon_{xy} \end{pmatrix}. \tag{3.8}$$

Here the convention to denote the elastic constants by c_{mn} was used, where m and n are defined as 1 = *xx*, 2 = *yy*, 3 = *zz*, 4 = *yz*, 5 = *xz*, 6 = *xy* and of course due to symmetry 4 = *zy*, 5 = *zx*, 6 = *yx*. We see that all the 36 elastic constants are independent. For crystals, many of them are the same due to symmetry restriction. For instance, in an orthorhombic crystal there are 9 different moduli (c_{11}, c_{22}, c_{33}, c_{12}, c_{13}, c_{23}, c_{44}, c_{55}, c_{66}); in tetragonal crystal, there are 6 moduli. For other crystal systems, the elastic constants are summarized in Table 3.1.

Table 3.1: Independent elastic constants for different crystal symmetries. Compare [10].

Crystal class	Number of c_{ij}	List of elastic constants
Triclinic	21	All possible combinations
Monoclinic	13	c_{11}; c_{12}; c_{13}; c_{16};c_{22}; c_{23}; c_{26}; c_{33}; c_{36}; c_{44}; c_{45}; c_{55}; c_{66}
Orthorhombic	9	c_{11}; c_{12}; c_{13}; c_{22}; c_{23}; c_{33}; c_{44}; c_{55}; c_{66}
Trigonal	6 or 7	c_{11}; c_{12}; c_{13}; c_{14}; c_{25}; c_{33}; c_{44};
Tetragonal	6	c_{11}; c_{12}; c_{13}; c_{33}; c_{44}; c_{66}
Hexagonal	5	c_{11}; c_{12}; c_{14}; c_{44};
Cubic	3	c_{11}; c_{12}; c_{44};
Isotropic	2	c_{11}; c_{44}

3.2 Propagating Stress Waves

Propagating stress waves are just elastic waves of various types such as longitudinal, transverse, surface and more. Solids support such a variety of stress waves, now we consider an elastic wave in a long, thin bar with cross-section area A and density ρ (Figure 3.5). Look at a segment width dx at point x and the elastic displacement u. According to *Newton's Second Law* we have

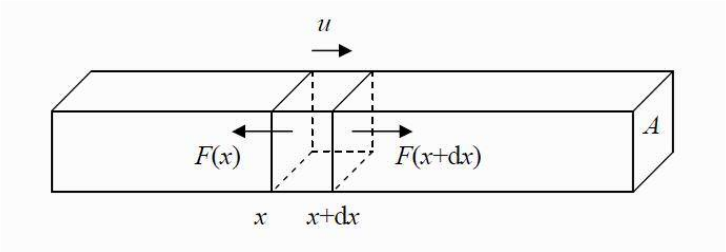

Figure 3.5: A long thin bar of cross-section A and density ρ. Figure taken from [8].

$$\rho A \mathrm{d}x \frac{\mathrm{d}^2 u}{\mathrm{d}t^2} = F(x + \mathrm{d}x) - F(x), \tag{3.9}$$

$$\rho \frac{\mathrm{d}^2 u}{\mathrm{d}t^2} = \frac{1}{A} \frac{\mathrm{d}F}{\mathrm{d}x} = \frac{\mathrm{d}\sigma_{xx}}{\mathrm{d}x}. \tag{3.10}$$

Assuming that the wave propagates along the x-direction we obtain $\sigma_{xx} = c_{11}\varepsilon_{xx}$, where c_{11} is here Young's modulus. Since $\varepsilon_{xx} = \frac{\mathrm{d}u}{\mathrm{d}x}$, this leads to

$$\frac{\mathrm{d}^2 u}{\mathrm{d}t^2} = \frac{c_{11}}{\rho} \frac{\mathrm{d}^2 u}{\mathrm{d}x^2}. \tag{3.11}$$

which is the *wave equation* for a long, thin bar. A solution of the wave equation has the form of a *propagating longitudinal wave* (each atom moves parallel to the direction of the wave vector) [11]

$$u(x,t) = u_0 e^{i(kx - \omega t)}, \tag{3.12}$$

where

$$v_L = \frac{\omega}{k} = \sqrt{\frac{c_{11}}{\rho}} \tag{3.13}$$

is the Young's modulus longitudinal speed of sound [8].

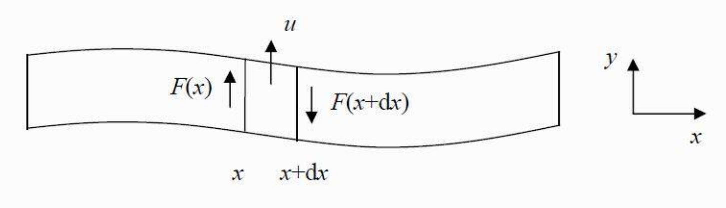

Figure 3.6: A long thin bar of cross-section A and density ρ. Figure taken from [8].

Similar analysis for transverse waves, in this case, we have

$$\rho\frac{\mathrm{d}^2u}{\mathrm{d}t^2} = \frac{\mathrm{d}\sigma_{xy}}{\mathrm{d}x}, \tag{3.14}$$

where the shear stress $\sigma_{xy} = c_{44}\varepsilon_{xy}$ with $\varepsilon_{xy} = \dfrac{\mathrm{d}u}{\mathrm{d}x}$. Therefore, we obtain the wave equation

$$\frac{\mathrm{d}^2u}{\mathrm{d}t^2} = \frac{c_{44}}{\rho}\frac{\mathrm{d}^2u}{\mathrm{d}x^2} \tag{3.15}$$

and the solution for this *propagating transverse wave* is:

$$u(x,t) = u_0e^{i(kx-\omega t)}, \tag{3.16}$$

where

$$v_T = \frac{\omega}{k} = \sqrt{\frac{c_{44}}{\rho}}. \tag{3.17}$$

is the transverse speed of sound [8].

Using equation

$$\frac{3}{v_S^3} = \frac{2}{v_T^3} + \frac{1}{v_L^3} \tag{3.18}$$

after a measurement of the elastic constants c_{11} and c_{44} we can calculate the speed of sound and with equation (2.2), eventually we find the way to the investigation of the lattice thermal conductivity κ_l dependent on the temperature. Now we face a new question: how to measure the elastic constants c_{11} and c_{44}. We will talk about this question in next chapter.

Chapter 4

Resonant Ultrasound Spectroscopy

As indicated before, we only have the last problem: how to measure the elastic constants c_{11} and c_{44}. In this chapter, we will introduce Resonant Ultrasound Spectroscopy, an elegant method of measuring the elastic tensor of a material.

4.1 Introduction

Resonant Ultrasound Spectroscopy (RUS) is a modern nondestructive evaluation technique for modulus measurements. It uses resonance frequencies corresponding to normal modes of a vibrating elastic body to infer its elastic constants. The samples are usually polished and made as a cube, parallelepiped, sphere or short cylinder. If the dimensions and mass are given, the complete elastic tensor can be inferred from a single measurement.

4.2 Measurement Principle

Figure 4.1 shows the classical experimental arrangement of RUS method. A sample was lightly placed between two transducers. A frequency synthesizer generates a wide range of frequencies and then the frequencies are emitted from one simple piezo-electric transducer. So the first transducer excites an elastic wave of a constant amplitude and varying frequency in the sample, while the second is used to detect the sample's mechanical response in an ultrasonic frequency band. If the incoming generated wave matches a natural frequency of the sample, it oscillates resonantly and a peak can be detected

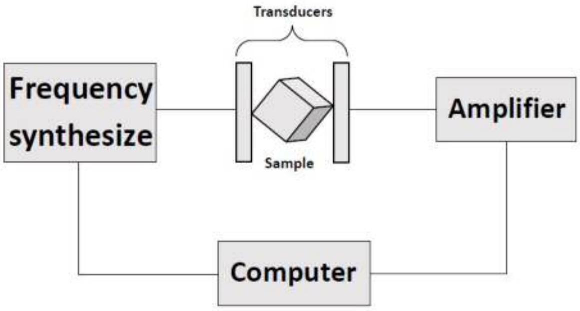

Figure 4.1: A schematic of classical experimental arrangement of RUS method.

at this frequency. Then we find every single resonance frequency from a measured spectrum (Figure 4.2). Calculation of the resonance frequencies of a sample is possible if its mass, dimensions, and estimated elastic moduli are known. Eventually, a computer program (based on the Levenberg-Marquardt algorithm) can accurately extract elastic moduli by fitting the calculated frequencies most closely to the measured resonance frequencies, which will be discussed in the next section.

4.3 Data Analysis

So far, we have discussed how we measure a sample with RUS method, but what is the principle of this data analysis of the RUS method actually?
In order to extract useful information (here the elastic constants) using RUS, two steps are necessary:

- Computation of resonance frequencies of our sample.
- Fitting the computation to our experiment.

Unfortunately, a complete solution of this problem in an analytical form does not exist. Thus, a non-analytic solution is required. Two methods could be used for this computation and analysis:

- Finite-element methods.
- Energy minimization techniques.

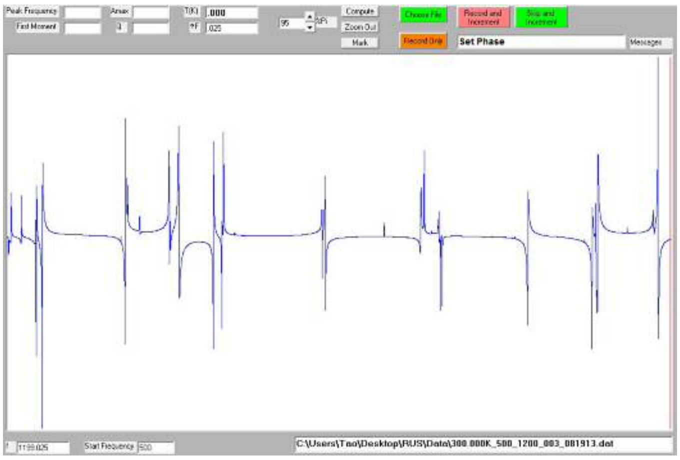

T(K) .000

°F .025

Start Frequency 500

1199.025

C:\Users\Tao\Desktop\RUS\Data\300.000K_500_1200_003_081913.dat

Figure 4.2: A spectrum of sample $Mg_2Si_{0.4}Sn_{0.6}$ obtained by RUS at room temperature, where x- and y-axis represent the frequency range and detected signal amplitude, respectively. Here the frequency range is from 500 kHz to 1200 kHz.

Indeed minimization techniques are dominating the RUS method. From classical mechanics, the general form of Lagrangian is written as

$$L = \int\limits_V (E_k - E_p) dV, \tag{4.1}$$

where E_k is the kinetic energy and E_p is the potential energy. For an elastic solid with volume V bounded by a surface S with density ρ, elastic tensor c_{ijkl} and a angular frequency of the normal modes ω, the kinetic energy and potential energy are given by

$$E_k = \frac{1}{2} \sum_i \rho \omega^2 u_i^2, \tag{4.2}$$

$$E_p = \frac{1}{2} \sum_{i,j,k,l} c_{ijkl} \frac{\partial u_i}{\partial x_j} \frac{\partial u_k}{\partial x_l}, \tag{4.3}$$

where every index runs over all 3 spacial directions and u_i is the corresponding component of the displacement vector. Using the variational principle, i.e. $\delta L = 0$ with arbitrary δu_i in V and on S, we obtain the condition

$$\rho \omega^2 u_i + \sum_{j,k,l} c_{ijkl} \frac{\partial^2 u_k}{\partial x_j \partial x_k} = 0 \tag{4.4}$$

which connects the resonance frequencies with the elastic tensor.

For further analysis, we expand the displacement vector u_i in a series of polynomial basis functions. Eventually, one can derive an eigenvalue equation in the form of

$$\omega^2 \mathbf{E} \vec{a} = \mathbf{\Gamma} \vec{a}, \tag{4.5}$$

where $\vec{a}$ is a vector corresponding to the displacement vector in the chosen basis and the two matrices $\mathbf{E}$ and $\mathbf{\Gamma}$ incorporate the corresponding terms of the former equation (4.4). For further information, please see [9].

Given the density, dimensions, and initially estimated elastic constants, equation (4.5) can be solved by standard numerical techniques. The solution of this eigenvalue equation gives the free-oscillation frequencies. So far, a significant accomplishment is achieved, but the most powerful ability of RUS method is then working backward to determine the accurate elastic constants by continuously adjusting the elastic constants until the calculated resonance frequencies match the experiment. During this investigation, the data analysis program is based on [9] and more detailed information about the program can be found in [9]. For a measurement of a polycrystalline rectangular parallelepiped sample, which we are working with, good fits have a root mean square error (abbreviated RMS or rms) of less than 0.05%

Chapter 5

Experimental Setup

After we figure out how elastic constants can be measured, our work of measurement should be moved into implementation now. This chapter provides a detailed description about our experimental setup.

5.1 Apparatus and Materials

Since the elastic properties of a material depend on temperature, the purpose of this investigation is to determine the elastic constants c_{11} and c_{44} of our samples from room temperature to a high temperature with a high-temperature RUS measurement system. A good preparation of samples is very important. In this investigation, we are interested in two different polycrystalline materials: p-type semiconductor material $\mathrm{MnSi}_{1.85}$ and n-type semiconductor material $\mathrm{Mg_2Si_{0.4}Sn_{0.6}}$. Usually the samples are processed into rectangular parallelepiped by cutting and polishing. Before we start the measure measurement, we should also first check if the samples have any visible defects. Figure 5.1 shows the picture of the high-temperature RUS measurement system used during this investigation. The measurement system contains a classical experimental arrangement of RUS method which was described before in Chapter 4, a furnace which heats the sample in the quartz tube from room temperature to high temperature and a temperature measuring device. To reduce vibrational interference, a vacuum pump is also required to create a vacuum environment for the sample. The essential parts of this apparatus are the buffer rods, which transfer the ultrasonic signal from the transducers to the sample. This is mandatory for high temperature measurement, since the transducers could be destroyed otherwise. For further details concerning this implementation please see [12] and for high temperature RUS please see [10]. The temperature of the sample was measured suing a type-K thermocouple nearby the sample position. Furthermore, the alumina discs, which can be seen in Figure. 5.1 (nearby the arrow denoting "Quartz tube") serve as heat shields.

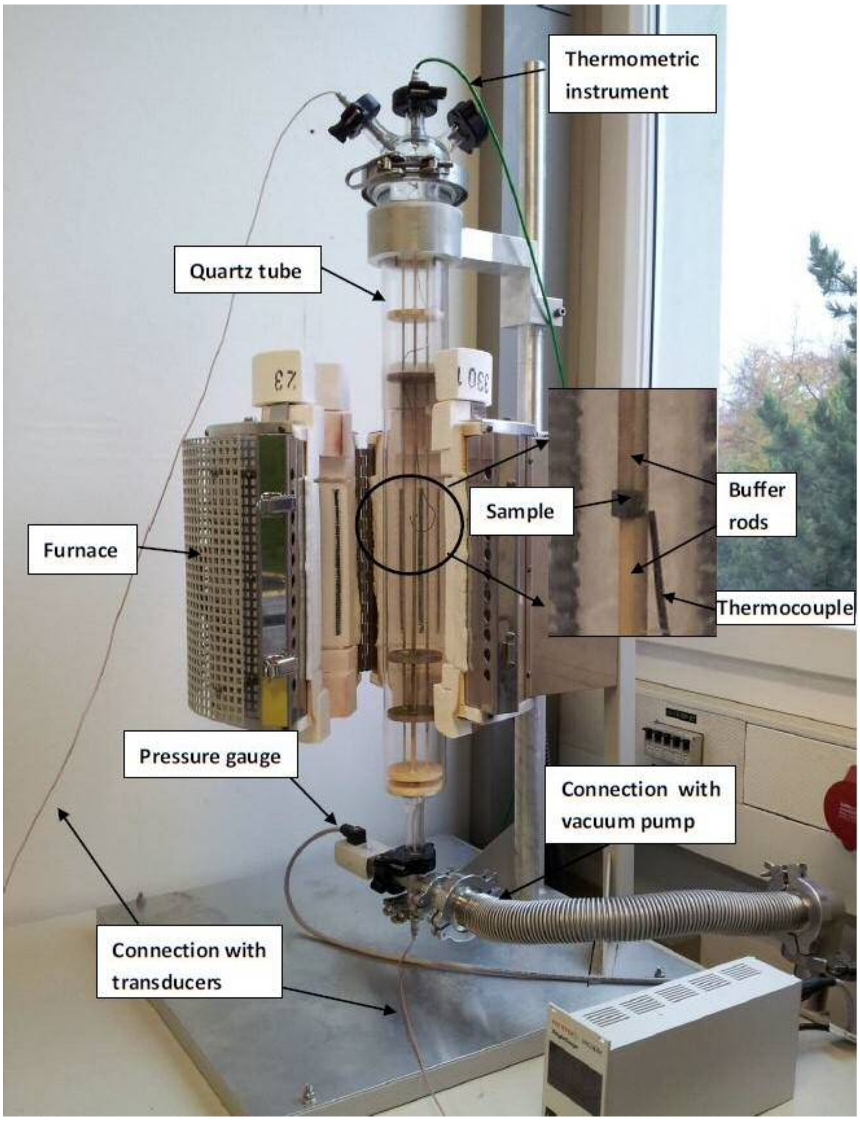

Figure 5.1: High-temperature RUS measurement system used during this investigation.

5.2 Control Program

In this investigation, the graphical environment *National Instruments LabVIEW* is used to control the furnace, i.e. to set temperature and record the temperature measured by a type-K thermocouple.

LabVIEW is a system-design platform developed by *National Instruments* and is commonly used for device control and data acquisition. The main advantage of *LabVIEW* is its graphical programming language (usually is called G programming language). Compared to general text-based programming languages like *C* and *Java*, G programming language uses “connecting wires” to connect graphical icons in block diagram and build up relationships between them, so G code is easier to quickly learn and understand.

The program written in G programming language is called virtual instrument which is most fundamental element of *LabVIEW* program. Dragging and connecting graphical icons creates a virtual instrument and this can be also used in other virtual instruments serving as sub-virtual instrument. Another characteristic of G language different from text-based programming language is that its program is implemented linearly, which means that the next command is implemented after the previous has been finished [11]. For instance, we take a look at the block diagram of *Keithley Read Temp* (Figure 5.2). The flat sequence structure contains 5 frames and each frame contains a graphical icon with different function. The first frame contains a case structure. If the case is true, then a function of GPIB initialization will be implemented. After the command in the first frame has been finished, the command in the second frame is then executed. Here a DevClear function is executed. It requires the address of GPIB device. If the address inputted is

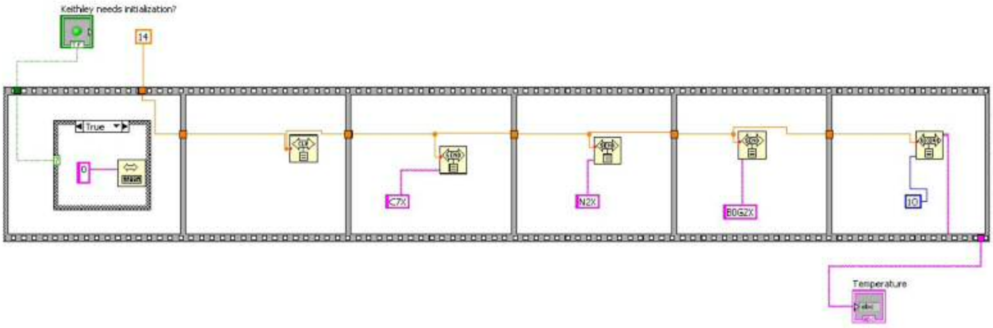

Figure 5.2: Block diagram of Keithley Read Temp.vi.

correct, the command in the third frame will be executed. It will continue until the command in the last frame is finished. In the end, the program will read data bytes from a GPIB device, i.e. the temperature will be read and displayed.

For our program designed with *LabVIEW*, following aspects should be considered:

- We input a series of set temperatures, then the program will control the furnace to reach corresponding temperatures and detect if the sample temperature is constant.
- After the sample temperature is constant, monitor the temperature and take a measurement.
- When a measurement is finished, continue and take next measurement at next set temperature. Moreover,

Below is a calibration curve of the furnace used during this investigation. From this figure, we see that after the temperature has been set, the sample

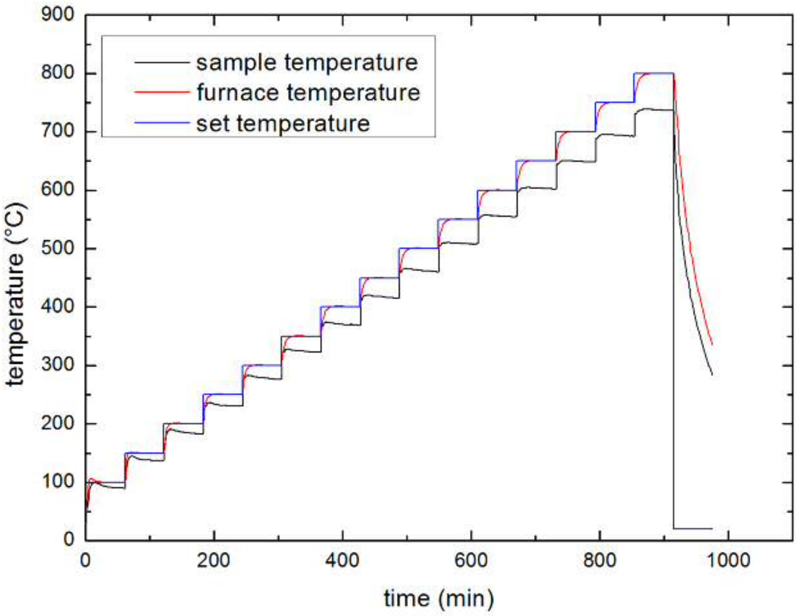

Figure 5.3: Calibration curve of the furnace.

temperature increases quickly and then slowly decreases. It will take a long time until the sample temperature is constant (here it is about 70 minutes.). Therefore, in our investigation we take a measurement of the sample temperature in every 10 minutes. We notice also that the sample temperature is usually lower than the corresponding set temperature. Take a look at Figure 5.1, the quartz tube absorbs energy from the furnace while it radiates energy to the room environment. So after equilibrium, its temperature should be lower than furnace temperature and that's why the temperature of sample in the quartz tube is lower than the corresponding set temperature. Moreover, the furnace temperature was actually measured closer to the set temperature as compared to the sample temperature sensor.

In our program, which is used to detect and ensure the sample temperature stays constant, we take following steps:

- We measure the sample temperature $T = T_{1s}$ at time $t = t_1$.
- After 10 minutes, we measure the sample temperature again $T = T_{2s}$ at time $t = t_1 + 600$ s.
- Compare T_{1s} and T_{2s}.

If the two temperatures are equal within a certain precision, which means the temperature doesn't change in this time interval, we conclude that that the temperature is now constant. We take a measurement at this time and record the sample temperature, then continue measuring until all measurements are completed.

With these considerations, a flow chart (Figure 5.4) is designed. Following this flow chart, we designed our computer program with *LabVIEW*.

Figure 5.5 shows the front panel of our program. In the frame of “Temperature Control”, we can input a series of the set temperatures and see the value of current set temperature. In the frame of “RUS Control” we can control the frequency range and number of data points. Because our measured data should also be saved, so a data root directory is also designed. In the frame of “Internal Data”, we can read the sample temperature. “Temperature 1” and “Temperature 2” show the sample temperature at different time (here the time difference is $t = 600$ s).

In Figure 5.6 the actual *LabVIEW* implementation is shown. Key elements are:

1. The iteration of the different set temperature.
2. The check for constant temperature and record the data of time, temperature.
3. RUS program as sub-virtual instrument.

5.3 A Test for Fused Quartz

Before the measurement of $Mg_2Si_{0.4}Sn_{0.6}$ and $MnSi_{1.85}$, we first took a test measurement using a fused quartz sample at room temperature with dimensions of 2.3 mm × 3.3 mm × 4.7 mm, density of 2.2 g/cm^3 and estimated elastic moduli $c_{11} = 75$ GPa and $c_{44} = 33$ GPa. We set the frequency range from 500 kHz to 2500 kHz using 40000 data points. Using program (based on the Levenberg-Marquardt algorithm) we obtained the results: elastic constant $c_{11} = 77.66$ GPa and $c_{44} = 31.12$ GPa with an excellent RMS error of less than 0.1%. Experimental and literature values [14] are in good agreement. Thus, our setups works well.

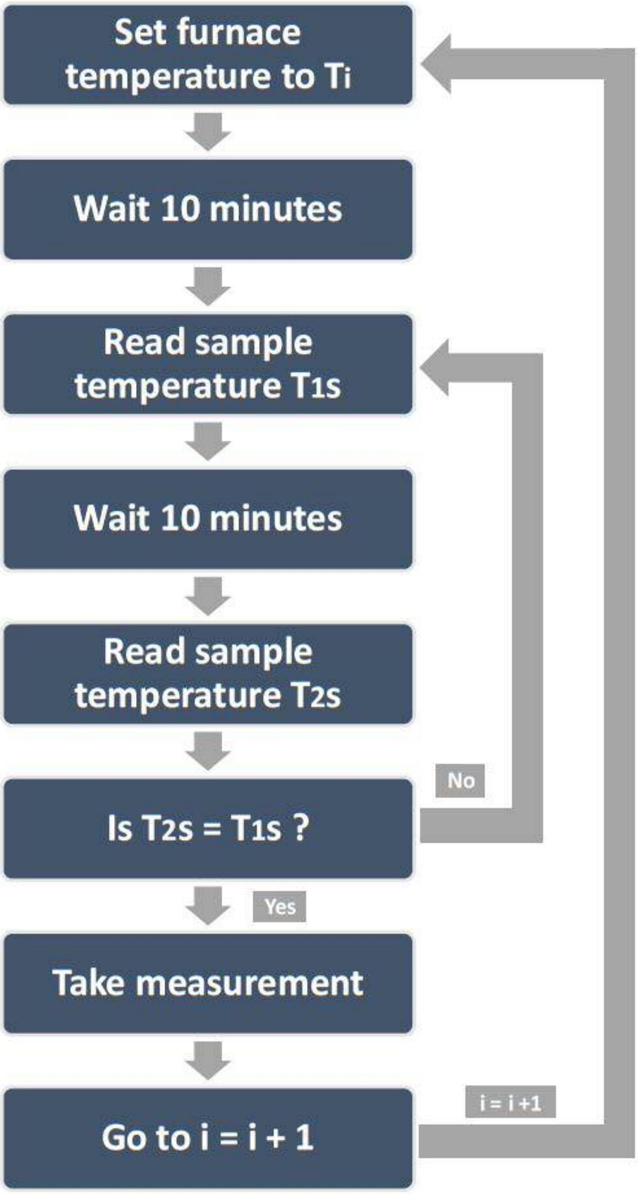

Figure 5.4: Flow chart for the control program. Here T_i is our set temperature. We first measure the sample temperature $T = T_{1s}$. After 10 minutes we measure the sample $T = T_{2s}$ temperature again.

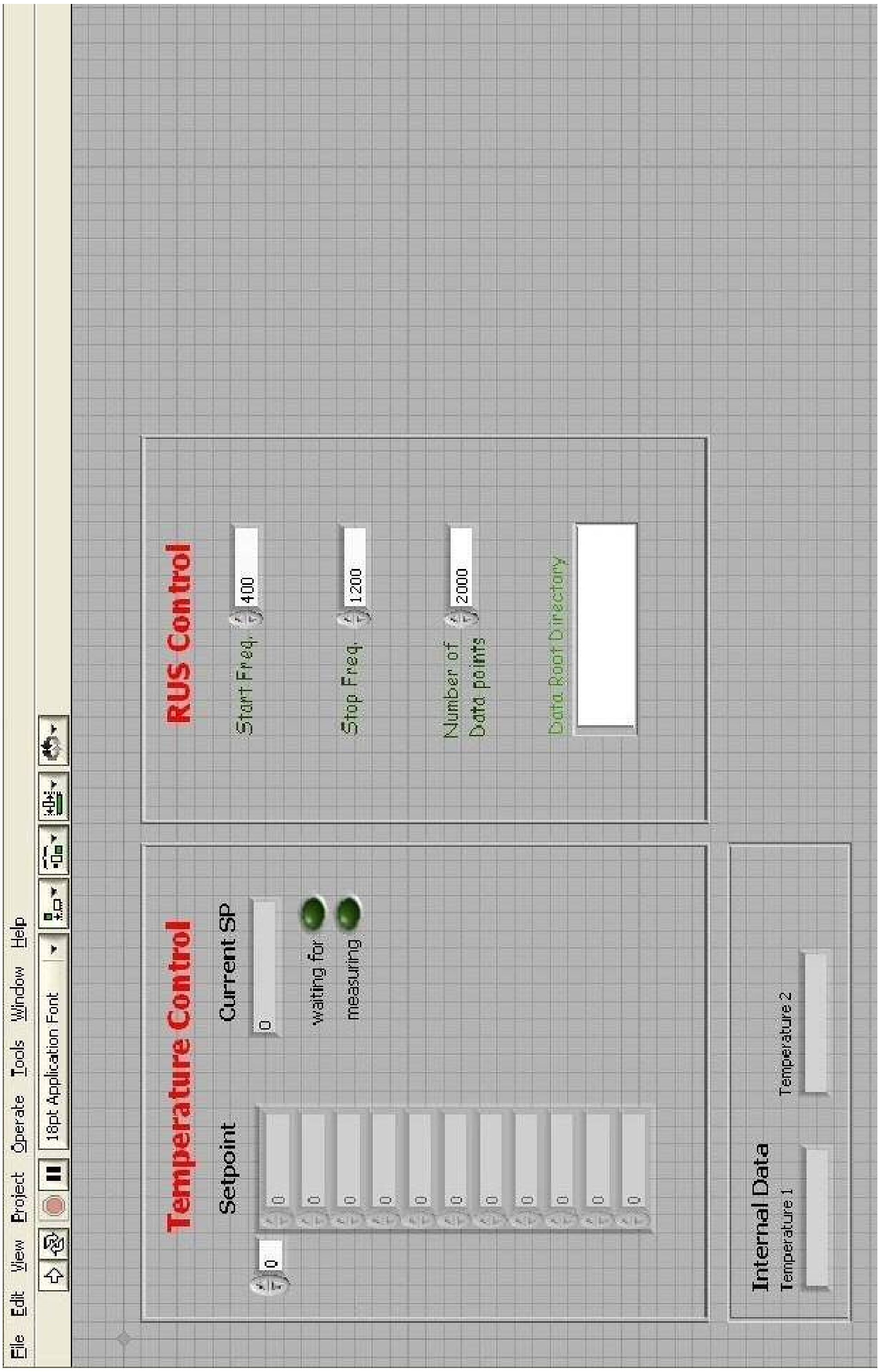

Setpoint 0

Current SP 0

Start Freq. 400

Stop Freq. 1200

Number of Data points 2000

Figure 5.5: Front Panel of our program in this investigation.

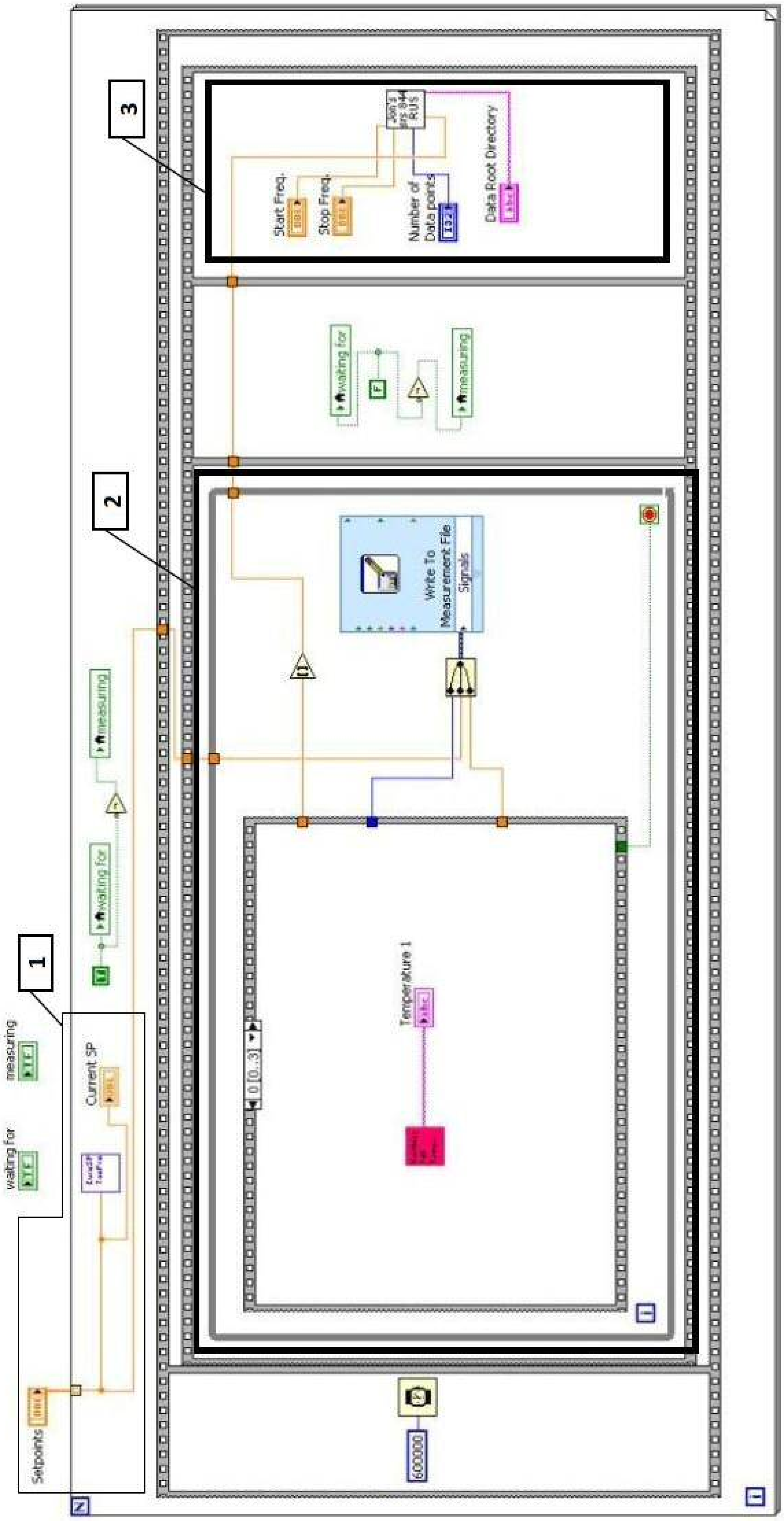

Figure 5.6: Block diagram of our program in this investigation.

Chapter 6

Results and Discussion

6.1 Measurement

In this investigation, we got 6 samples of n-type semiconductor material $Mg_2Si_{0.4}Sn_{0.6}$ and 3 samples of p-type semiconductor material $MnSi_{1.85}$ produced by Fraunhofer IPM [15]. Before we started the measurement, we first took several measurements for every sample with RUS at room temperature and analyzed their spectra. Selection criteria are resonance quality and amplitude, which e.g. may be affected by inclusions or voids due to the synthesis route. After selecting, we picked up sample #1 of $MnSi_{1.85}$ with dimensions 2.968 mm × 2.989 mm × 2.998 mm, density $\rho = 4.775$ g/cm^3 and elastic moduli $c_{11} = 280$ GPa and $c_{44} = 110$ GPa and sample #2 of $Mg_2Si_{0.4}Sn_{0.6}$ with dimensions 3.049 mm × 3.041 mm × 2.997 mm, density $\rho = 2.914$ g/cm^3 and estimated elastic moduli elastic moduli $c_{11} = 97$ GPa and $c_{44} = 37.2$ GPa (Figure 6.1) for our measurement.

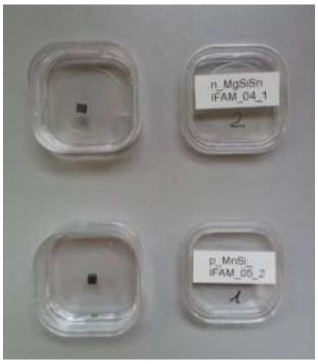

Figure 6.1: Samples of n-type semiconductor material $Mg_2Si_{0.4}Sn_{0.6}$ and p-type semiconductor material $MnSi_{1.85}$.

For sample $MnSi_{1.85}$, we take a frequency range from 500 kHz to 2000 kHz over a temperature range from room temperature to 834 K in steps of 25 K and use 30000 data points. For sample $Mg_2Si_{0.4}Sn_{0.6}$, the frequency range is from 500 kHz to 1200 kHz over a temperature range from room temperature to 613 K in steps of 25 K and the number of data points is 20000.

6.2 Results

6.2.1 For p-type semiconductor material $MnSi_{1.85}$

The resonant frequencies that could be detected from 500 kHz to 2000 kHZ over the whole temperature range for the sample $MnSi_{1.85}$ are shown in Figure 6.2. We can see that the resonant frequencies continuously decreased. Moreover, during our investigation, it was difficult to determine the resonance frequencies in high-temperature measurements. From the experimental point of view, it is possible that samples and buffer rods slightly move due to thermal expansion resulting in a worse mechanical contact between them and usually, the strength of acoustic resonance of most materials becomes weaker with increasing temperature. In these measurements, our fit RMS errors for resonant frequencies were between 0.0688% and 0.1455%, which indicated a reasonable result.

The decreasing values of resonant frequencies were directly related to the determined temperature dependent elastic constants (see Figure 6.3) which were calculated using the resonant frequencies as described in section 4.3. With equation (4.4), we realize that if the resonant frequencies decreases, the corresponding elastic moduli will also decrease. It is a typical consequence of lattice softening [11]. For analysis, we take a look at harmonic oscillator: an object with mass m connected to a spring with spring constant k. We know its resonant frequency $f = \omega/2\pi$ with $\omega = \sqrt{k/m}$. We realize the spring constant k decreases with decreasing resonant frequency. Here k is analogous to the elastic constant because in a solid-state model, the atoms are bond together as if they are connected by springs. For insurance purpose, we estimated the RMS error for elastic constants with 1% because the fit RMS errors for resonant frequencies are not the real RMS errors for the elastic constants.

Using equation (3.13), (3.17) and (3.18), we calculated the corresponding longitudinal and transverse speed of sound as well as the overall speed of sound shown in Figure 6.4. Over the investigated temperature range, the speed of sound decreased about 4%. Since the determined elastic constants are quite close to the literature values for the monosilicide MnSi [16], the data presented here are quite reasonable.

In general, the total thermal conductivity of higher manganese silicide is expected to stay relatively constant from room temperature to about 900K [17], which was also experimentally confirmed for this specific sample [15]. Therefore, the reduction of lattice thermal conductivity κ_l of about 8% (calculated using equation (2.2)) due to the speed of sound reduction of 4% must be compensated by most likely electronic thermal conductivity κ_e. In any case, this investigation confirmed that the lattice contribution to the temperature dependence of thermal conductivity is rather small.

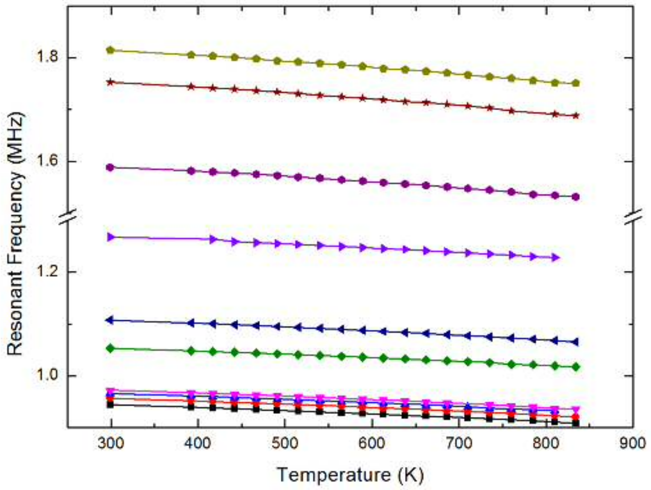

Figure 6.2: Resonant frequencies of $MnSi_{1.85}$ from room temperature to 834 K. In this investigation, 10 common resonant frequencies were found and tracked throughout the temperature range.

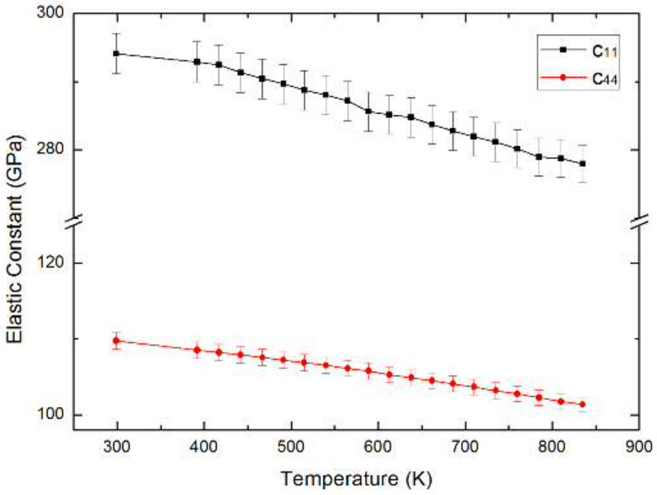

Figure 6.3: Elastic constants c_{11} and $c_{44}$of $MnSi_{1.85}$ from room temperature to 834 K.

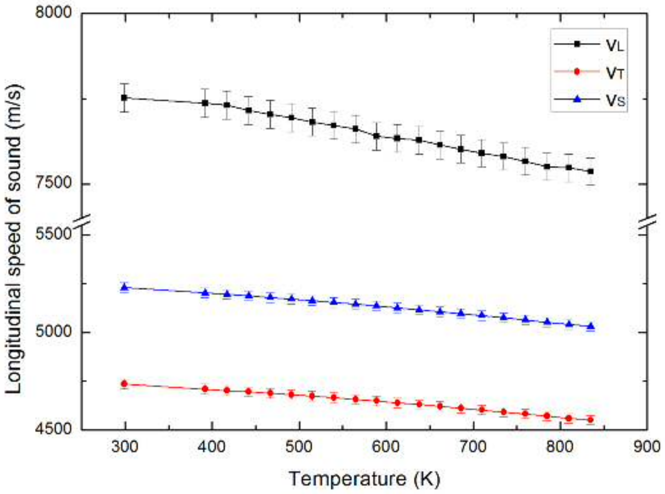

Figure 6.4: This figure shows the longitudinal speed of sound v_L, transverse speed sound v_T and overall speed of sound v_S from room temperature to 834 K.

6.2.2 For n-type semiconductor material $Mg_2Si_{0.4}Sn_{0.6}$

For the measurement of sample $Mg_2Si_{0.4}Sn_{0.6}$, we selected a frequency range from 500 kHz to 1200 kHz. Figure 6.5 shows the resonant frequencies that could be detected over the whole temperature range from room temperature to 613 K. In these measurements, our fit RMS errors for resonant frequencies were between 0.0753% and 0.1639%, which indicated also a reasonable result. The resonant frequencies of this sample decrease also with increasing temperature. Therefore, as indicated before, its elastic constants should also decrease which are shown in Figure 6.6. Using equation (3.13), (3,17) and (3.18), we calculated the corresponding longitudinal, transverse and overall speed of sound of this sample shown in Figure 6.7. Its experimental elastic constants values at temperature are in very good agreement with literature values of $Mg_2Si_{0.5}Sn_{0.5}$ [18] and between the values of pure Mg_2Si and Mg_2Sn [19, 20].

From results, the overall speed of sound v_S reduced about 4% which means the lattice thermal conductivity reduced about 8%. In general, a further decrease of v_S is expected but the total thermal conductivity κ increases strongly above 600 K [15]. Therefore, in this case the electronic part of κ must dominate the thermal transport.

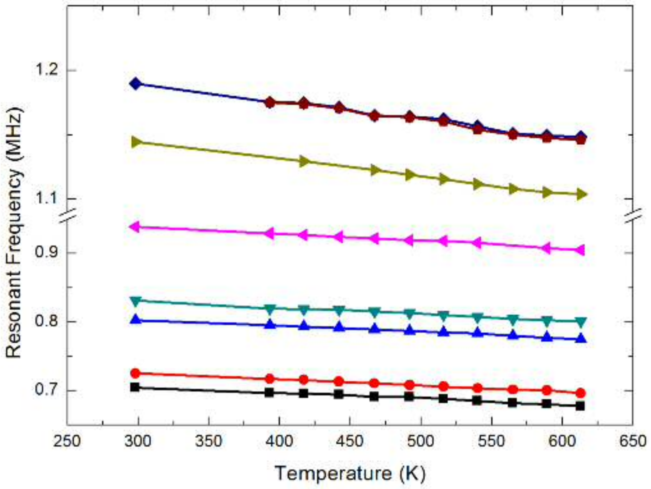

Figure 6.5: Resonant frequencies of $Mg_2Si_{0.4}Sn_{0.6}$ from room temperature to 613 K. In this investigation, 8 common resonant frequencies were found and tracked throughout the temperature range.

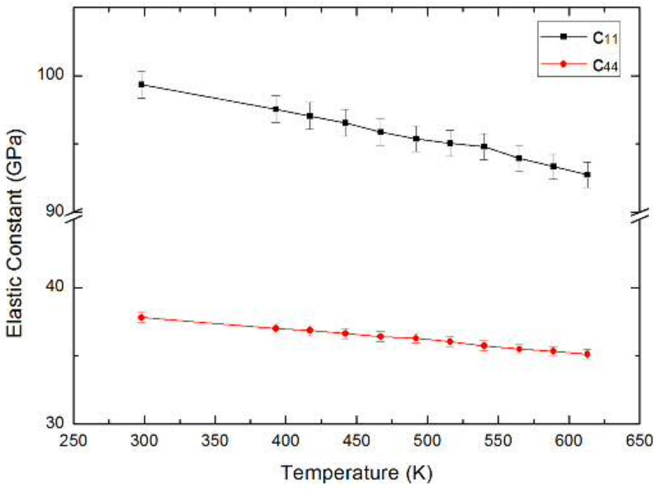

Figure 6.6: Elastic constants c_{11} and c_{44} of $Mg_2Si_{0.4}Sn_{0.6}$ from room temperature to 613 K.

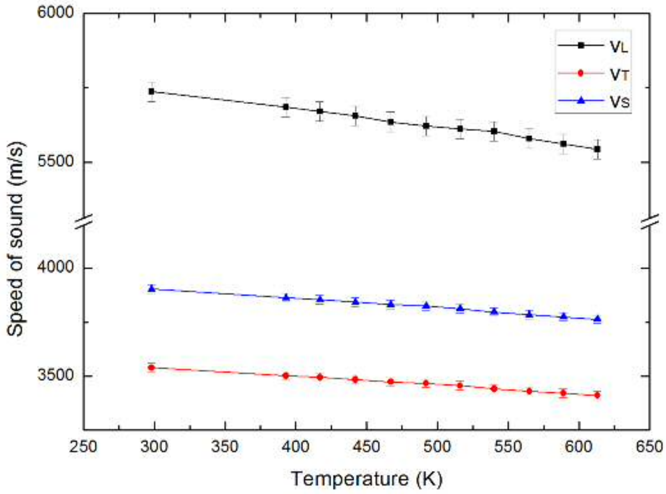

Figure 6.7: This figure shows the longitudinal speed of sound v_L, transverse speed sound v_T and overall speed of sound v_S from room temperature to 613 K.

Chapter 7

Conclusions

In this work, we have presented an experimental method for investigation of the temperature dependence of the lattice thermal conductivity κ_l at high temperatures. To control the temperature and make it easy for our measurement, a program was also developed in the lab during this investigation.

Using RUS, we measured the resonant frequencies of both silicides n-type semiconductor material $Mg_2Si_{0.4}Sn_{0.6}$ and p-type semiconductor material $MnSi_{1.85}$ from room temperature to high temperature. It is observed that the resonant frequencies of both materials decreased with increased temperature. Using the relationship between resonant frequencies and elastic constants, we confirmed that the elastic constants of both materials also decreased with increasing temperature. Eventually, we concluded that κ_l of both materials decreases 8% throughout the temperature range.

The experiment setup works quite well at room temperature. But at high temperature, it is hard to find resonant frequencies in the spectrum. Therefore, improvement of our high-temperature RUS measurement system is still required. We should improve the sensitivity of our transducers or give more powerful signals to the samples. Upon this work, further work can be also expanded. For instance, one can change the compositions of material $Mg_2Si_{0.4}Sn_{0.6}$ to $Mg_2Si_{0.3}Sn_{0.7}$ and take a new measurement.

Appendix A

Spectra for Sample MnSi$_{1.85}$

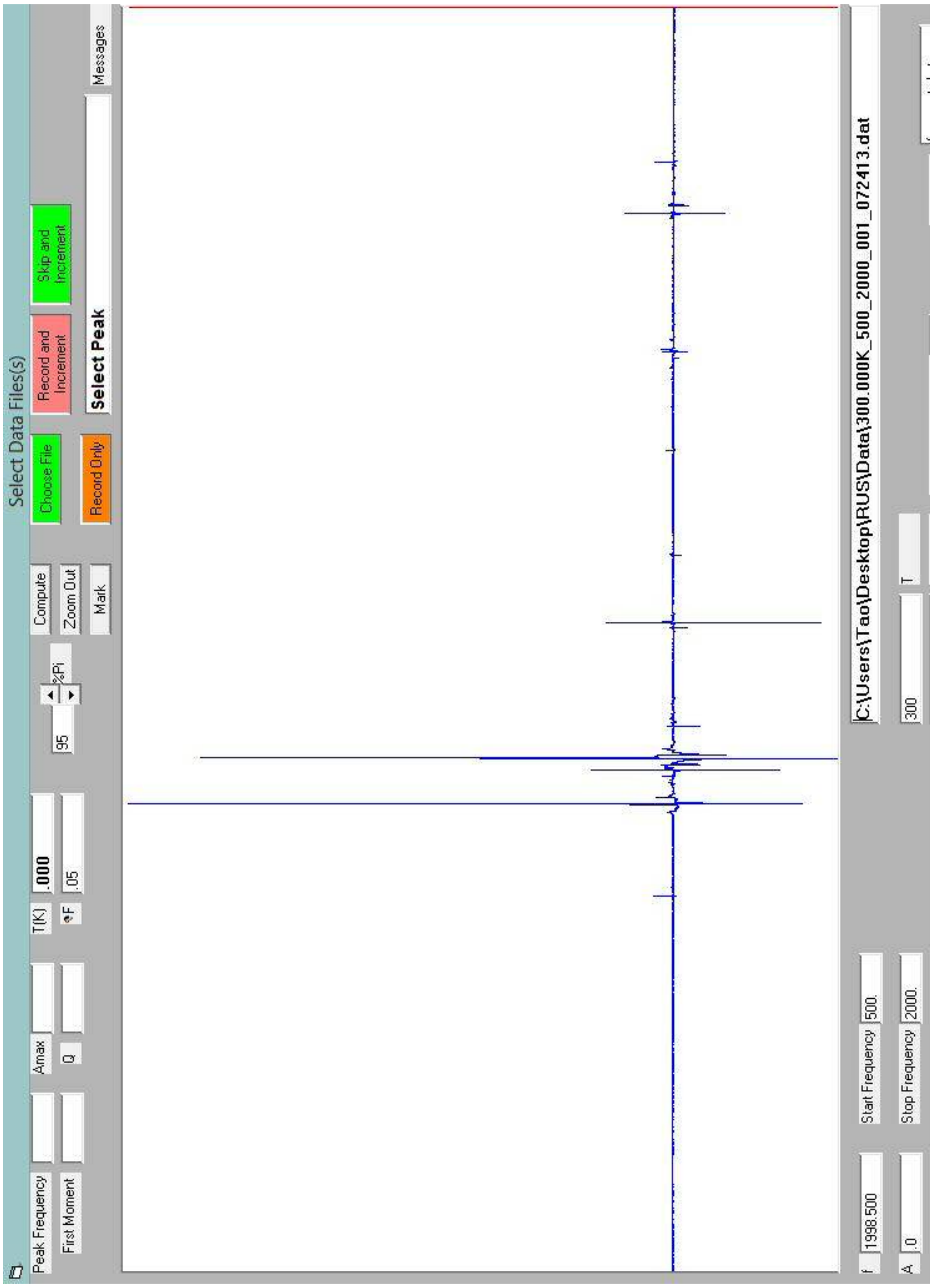

Peak Frequency

First Moment

Amax

Q

T(K) .000

δF .05

95 %Pi

C:\Users\Tao\Desktop\RUS\Data\300.000K_500_2000_001_072413.dat

f 1998.500

A .0

Start Frequency 500.

Stop Frequency 2000.

300

T

Figure A.1: A spectrum of sample MnSi$_{1.85}$ obtained by RUS, where x- and y-axis represent the frequency range and detected signal amplitude, respectively. Every peak represents a resonant frequency. Here the frequency range is from 500 kHz to 2000 kHz and temperature $T = 300$ K.

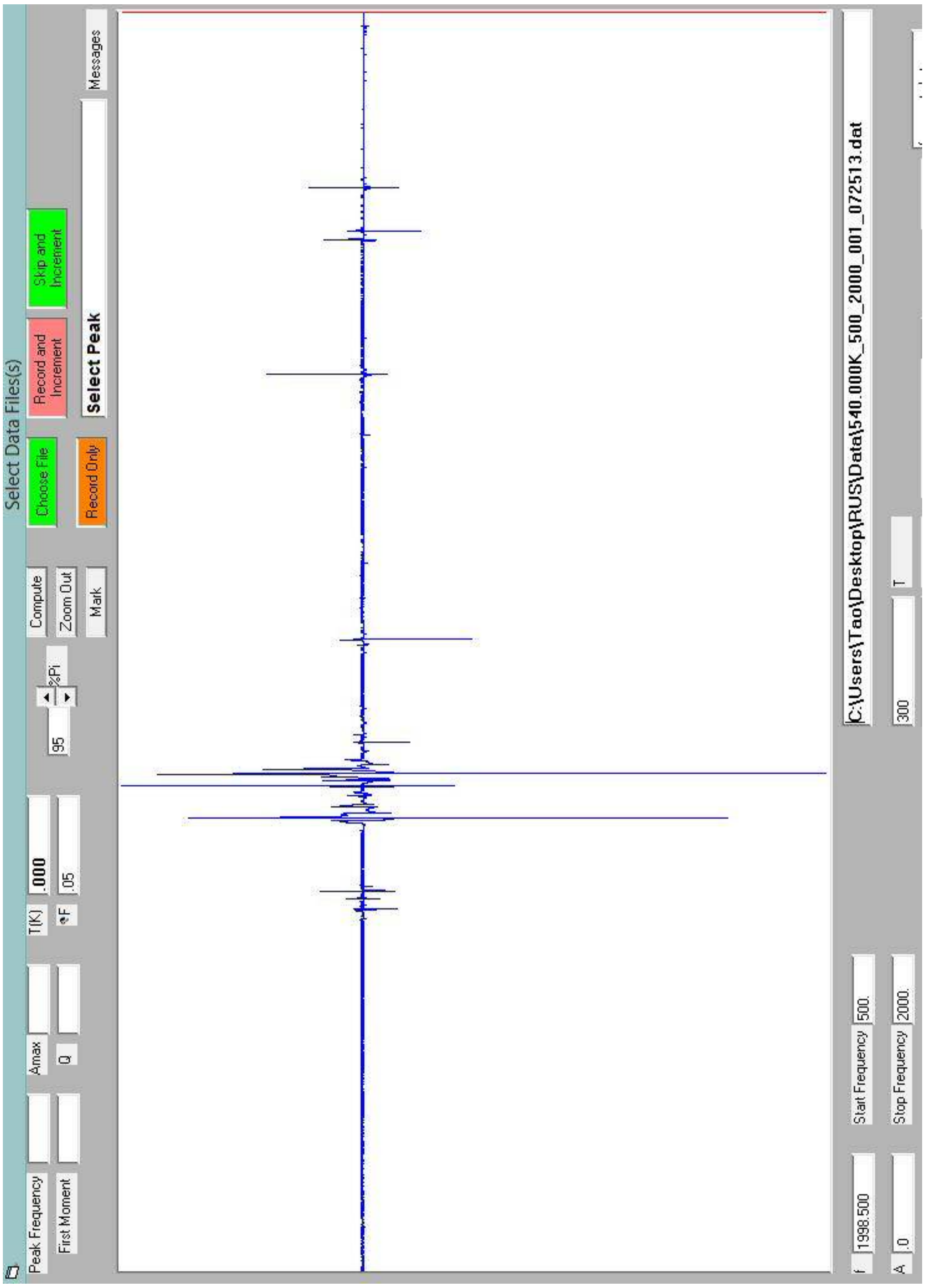

T(K) .000

δF .05

95 %Pi

C:\Users\Tao\Desktop\RUS\Data\540.000K_500_2000_001_072513.dat

f 1998.500

A .0

Start Frequency 500.

Stop Frequency 2000.

300

T

Figure A.2: A spectrum of sample $MnSi_{1.85}$ obtained by RUS, where x- and y-axis represent the frequency range and detected signal amplitude, respectively. Every peak represents a resonant frequency. Here the frequency range is from 500 kHz to 2000 kHz and temperature $T = 540$ K.

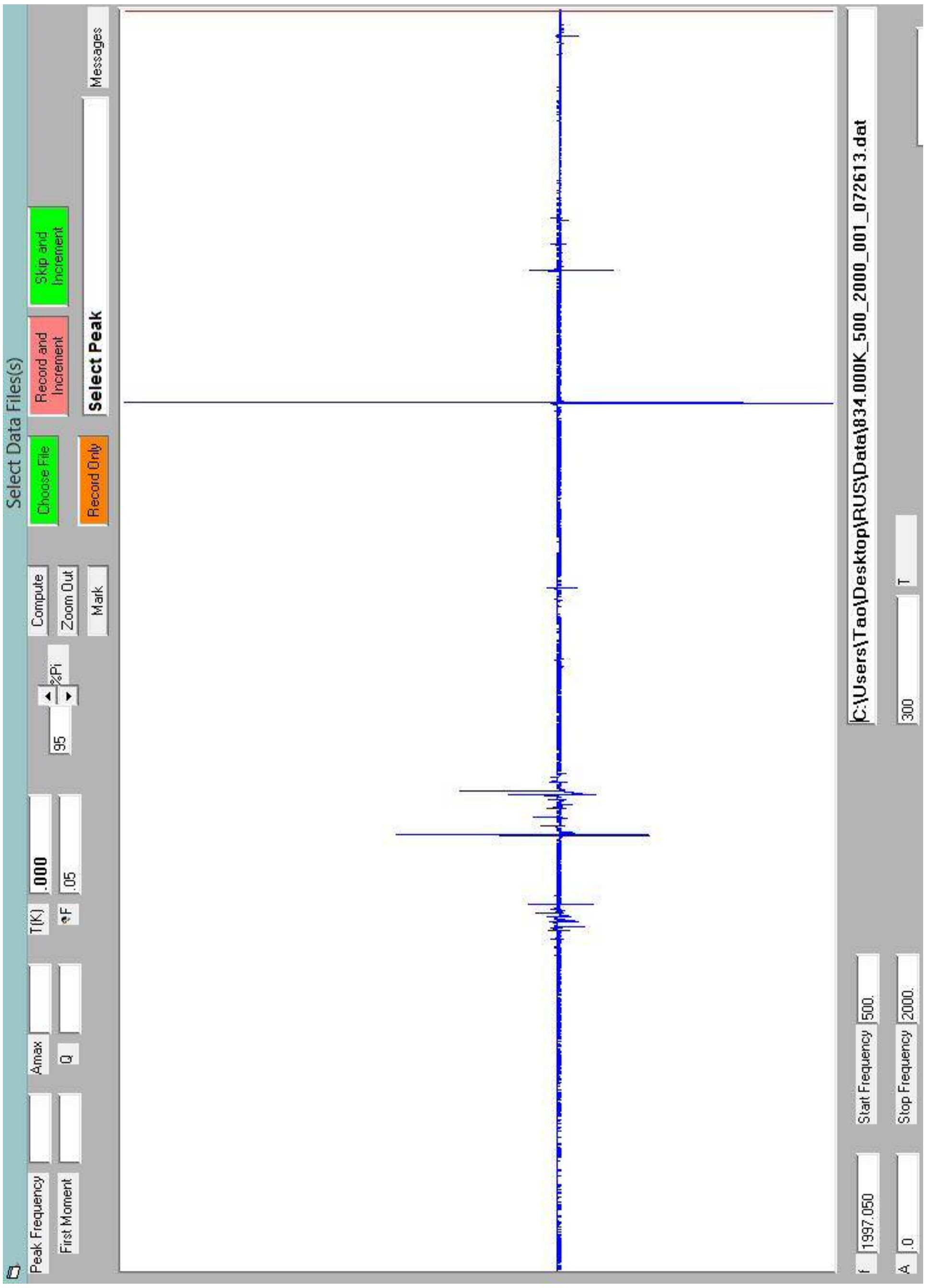

Peak Frequency

First Moment

Amax

Q

T(K) .000

F .05

95 %Pi

C:\Users\Tao\Desktop\RUS\Data\834.000K_500_2000_001_072613.dat

f 1997.050

A 0

Start Frequency 500.

Stop Frequency 2000.

300 T

Figure A.3: A spectrum of sample MnSi$_{1.85}$ obtained by RUS, where x- and y-axis represent the frequency range and detected signal amplitude, respectively. Every peak represents a resonant frequency. Here the frequency range is from 500 kHz to 2000 kHz and temperature $T = 834$ K.

Appendix B

Spectra for Sample $Mg_2Si_{0.4}Sn_{0.6}$

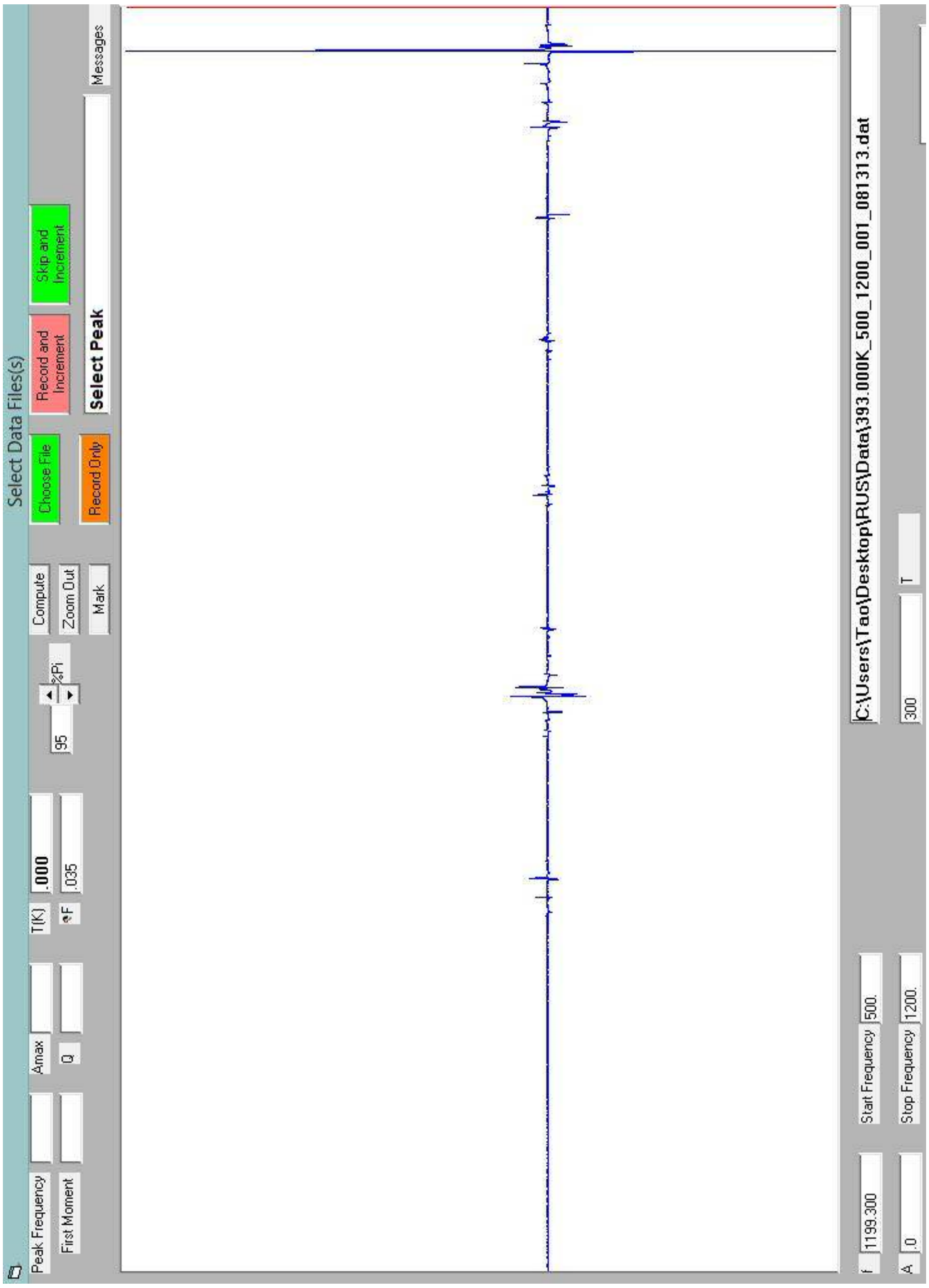

Peak Frequency
First Moment
Amax
Q
T(K) .000
F .035
95
C:\Users\Tao\Desktop\RUS\Data\393.000K_500_1200_001_081313.dat
300
T
Start Frequency 500.
Stop Frequency 1200.
f 1199.300
A .0

Figure B.1: A spectrum of sample $Mg_2Si_{0.4}Sn_{0.6}$ obtained by RUS, where x- and y-axis represent the frequency range and detected signal amplitude, respectively. Every peak represents a resonant frequency. Here the frequency range is from 500 kHz to 1200 kHz and temperature $T = 393$ K.

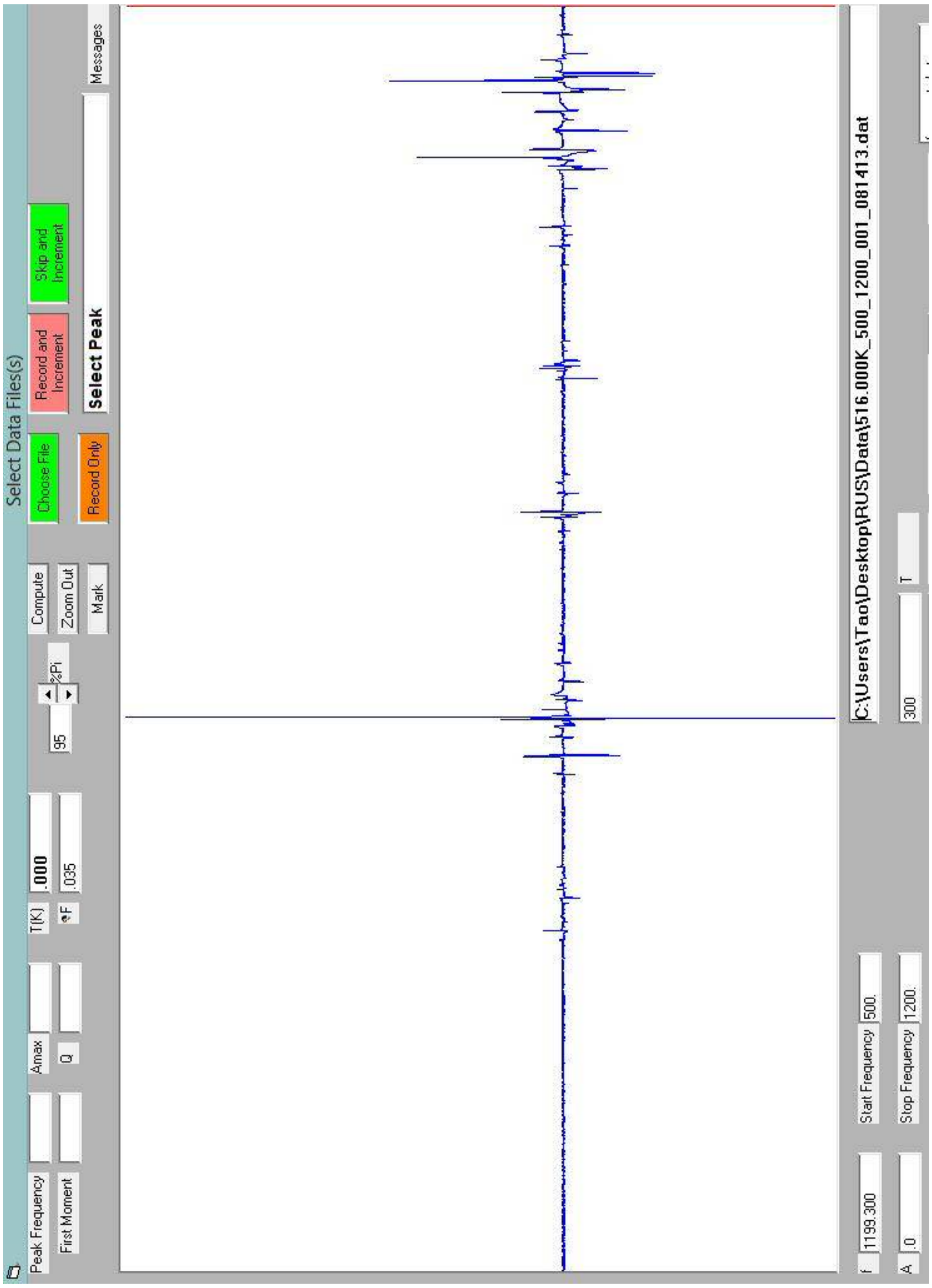

Peak Frequency

Amax

T(K) .000

First Moment

Q

ΔF .035

95 %Pi

C:\Users\Tao\Desktop\RUS\Data\516.000K_500_1200_001_081413.dat

f 1199.300

A .0

Start Frequency 500.

Stop Frequency 1200.

300

T

Figure B.2: A spectrum of sample $Mg_2Si_{0.4}Sn_{0.6}$ obtained by RUS, where x- and y-axis represent the frequency range and detected signal amplitude, respectively. Every peak represents a resonant frequency. Here the frequency range is from 500 kHz to 1200 kHz and temperature $T = 516$ K.

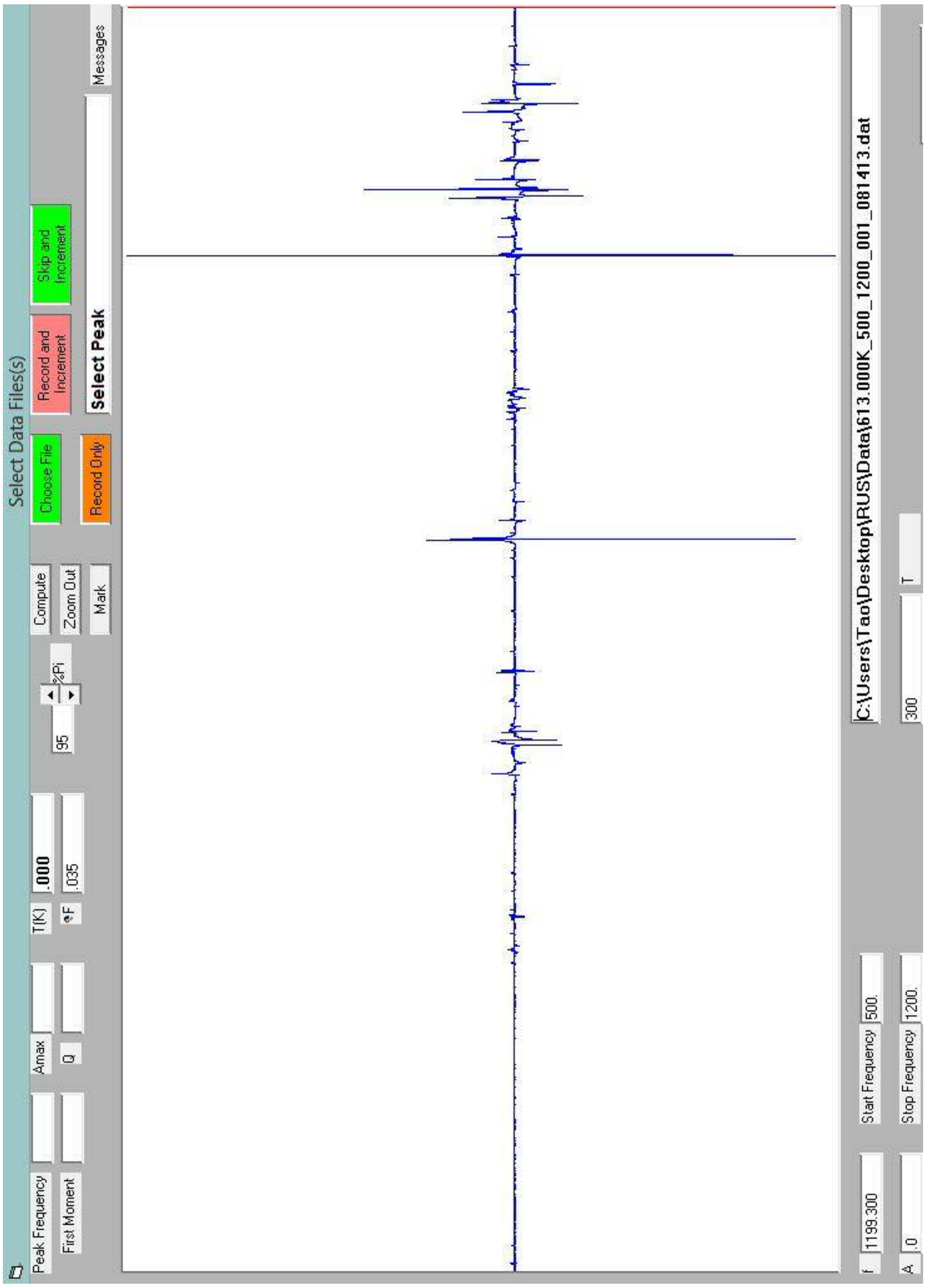

Peak Frequency

Amax

T(K) .000

First Moment

Q

δF .035

95 %Pi

C:\Users\Tao\Desktop\RUS\Data\613.000K_500_1200_001_081413.dat

f 1199.300

Start Frequency 500.

Stop Frequency 1200.

A .0

300

T

Figure B.3: A spectrum of sample $Mg_2Si_{0.4}Sn_{0.6}$ obtained by RUS, where x- and y-axis represent the frequency range and detected signal amplitude, respectively. Every peak represents a resonant frequency. Here the frequency range is from 500 kHz to 1200 kHz and temperature $T = 613$ K.

References

[1] D. M. Rowe, editor. *Thermoelectrics Handbook: Macro to Nano.* Taylor & Francis Group, 2006.

[2] M. I. Fedorov and V. K. Zaitsev. *"Thermoelectrics of Transition Metal Silicides" in Thermoelectric Handbook, edited by D. M. Rowe.* Taylor & Francis Group, 2006.

[3] R. P. Hermann. *"Thermoelectrics" in Electronic Oxides-Correlation Phenomena, Exotic Phases and Novel Functionalities,* Forschungszentrum Jülich, 2010.

[4] H. J. Goldsmid. *Introduction to Thermoelectricity.* Springer-Verlag Berlin Heidelberg, 2010.

[5] William Jones and Norman H. March. *Theoretical Solid State Physics.* Courier Dover Publications, 1986.

[6] Thermoelectric Generators, Washington State University. *http://e3tnw.org/ItemDetail.aspx?id=278*, last access on 03.01.2014.

[7] F. A. Carey. *On-Line Learning Center for "Organic Chemistry".* McGraw-Hill Companies.

[8] E. Y. Tsymbal. *Physics-927: Introduction to Solid State Physics* University of Nebraska-Lincoln.

[9] D. Gross, W. Hauger, J. Schröder, W. A. Wall and J. Bonet. *Mechanics of Materials.* Springer-Verlag Berlin Heidelberg, 2011.

[10] G. Li and J. R. Gladden. *High Temperature Resonant Ultrasound Spectroscopy: A Review.* International Journal of Spectroscopy, Vol. **2010**, 206362, 2010.

[11] A. Migliori and J. L. Sarrao. *Resonant Ultrosound Spectroscopy: Applications to Physics, Materials Measurements, and Nondestructive Evaluation.* John Wiley & Sons. Inc, 1997.

[12] Paula Bauer Pereira. *Structure and Lattice Dynamics of Thermoelectric Complex Chalcogenides.* Ph. D. - Thesis, University of Liege, 2012.

[13] *LabVIEW User User Manual.* National Instruments Corporation, 2004.

[14] A. Polian, Dung Vo-Thanh and P. Richet. *Elastic Properties of a-*SiO_2 *up to 2300K from Brillouin Scattering Measurements.* Europhys. Lett., **57**, 375, 2002.

[15] Dr. K. Tarantik, Fraunhofer IPM, Freiburg im Breisgau, Germany, 2013. Private communication.

[16] G. P. Zinoveva, L. P. Andreeva and P. V. Geld. *Elastic Constants and Dynamics of Crystal Lattice in Monosilicides with B20 Structure.* phys. stat. sol. (a) **23**, 711, 1971.

[17] P. Norouzzdeh, Z. Zamanipour, J. S. Krasinski and D. Vashaee. *The effect of nanostructuring on thermoelectric transport properties of p-type higher manganese silicide* $MnSi_{1.73}$. Journal Of Applied Physics **112**, 124308, 2012.

[18] Liu Na-Na, Song Ren-Bo and Du Da-Wei. *Elastic constants and thermodynamic properties of* $Mg_2Si_xSn_{1-x}$ *from first-principles calculations.* Chin. Phys. Soc. **18**, 1674, May 2009.

[19] Philippe Baranek and Joël Schamps. *Ab Initio Studies of Electronic Structure, Phonon Modes, and Elastic Properties of* Mg_2Si. J. Phys. Chem. B, **101**, 9147, 1997.

[20] L. C. Davis, W. B. Whitten and G. C. Danielson. *Elastic Constants and Calculated Lattice Vibration Frequencies of* Mg_2Sn. J. Phys. Chem Solids Vol. **28**, 439, 1967.